PNAS
www.pnas.org

Supplementary Information for

Strong methane point sources contribute a disproportionate fraction of total emissions across multiple basins in the U.S.

Daniel H. Cusworth[1,2*], Andrew K. Thorpe[3], Alana K. Ayasse[1,2], David Stepp[2], Joseph Heckler[4], Gregory P. Asner[4,2], Charles E. Miller[3], Vineet Yadav[3], John W. Chapman[3], Michael L. Eastwood[3], Robert O. Green[3], Benjamin Hmiel[5], David Lyon[5], and Riley M. Duren[1,2]

[1]Arizona Institutes for Resilience, University of Arizona, Tucson, AZ, USA
[2]Carbon Mapper, Pasadena, CA, USA
[3]Jet Propulsion Laboratory, California Institute of Technology, Pasadena, CA, USA
[4]Center for Global Discovery and Conservation Science, Arizona State University, Tempe, AZ, USA
[5]Environmental Defense Fund, Austin, TX, USA

*Corresponding Author: Daniel Cusworth
Email: dcusworth@arizona.edu

This PDF file includes:

Section S1. *Plume identification and source attribution protocols*

The plume discrimination and attribution approach closely resembles the methodology used in Cusworth et al. [1]. For plume identification, we generate full scene CH4 maps (Figure S7). These maps are used in conjunction with RGB imagery from the imaging spectrometer to identify the origin of plumes. A positive plume detection is recorded if a cluster of CH4 enhancements corresponds to a plume-like structure and if these enhancements are not exactly correlated to obvious surface confusers (e.g., rooftops, roads, water bodies, clouds, etc.). The origin of a positively identified plume corresponds to a region of high relative plume enhancement that corresponds to a plausible source location (e.g., tank battery, vent stack) as identified with comparison to available RGB layers.

For source attribution, we used a combination of these RGB layers (DIMAC (~60 cm) imagery, AVIRIS-NG/GAO RGB, Google Earth). Three human analysts followed the classification protocols:

- Sites were classified as “Production” if they were clearly associated with well pad infrastructure (well heads, pumpjacks, well completions, tanks at production sites). Sources that were visibly connected to tanks at production sites were labelled “tanks” while all other sites were labelled “well-site.”
- Sites were classified as “Gathering and Boosting” if they were clearly associated with gathering pipelines or any infrastructure within a compressor station’s footprint. For example, if a tank at a compressor station was detected as a source, it was labelled “compression.”
- Sites were classified as “Processing plants” if any sources were detected within the footprint of the processing plant.
- Sites were classified as “Gas power plants” if any sources were detected within the footprint of a gas power plant
- Sites were classified as “livestock” if any sources were detected at confined animal feeding operations (CAFOs), including manure lagoons and pits.
- Sites were classified as “landfills” if plume were detected within the active, intermediate, or final cover faces, or gas capture system within the footprint of a landfill.
- Sites were classified as “coal” if plumes were clearly emanating from coal mine vents or if large diffuse enhancements were detected from non-vent related coal infrastructure

Examples of classified sources are shown in Figure S8-S9. We show RGB imagery for each platform (DIMAC, AVIRIS-NG/GAO, Google Earth), and how the source was classified. Sources where a clear determination could not be made remained unlabeled. All plume imagery is available for visualization and download at carbonmapperdata.org

Section S2. *TROPOMI Flux Inversion*

Section S2.1 Inversion algorithm

We infer gridded CH4 emission fluxes using TROPOMI XCH4 over roughly the same time period as an airborne campaign. To ensure sufficient samples to constrain regional fluxes, we performed TROPOMI inversions for two months surrounding each campaign. We use the Stochastic Time-Inverted Lagrangian Transport model (STILT; [2]), driven by meteorological reanalysis wind fields. We use the High Resolution Rapid Refresh (HRRR) 3 × 3 km product, which is available at a 3 hourly time resolution (https://www.ready.noaa.gov/READYmetdata.php). The STILT model simulates an influence function or "footprint" at a receptor by releasing an ensemble of particles backwards in time along the winds. Receptors represent instantaneous atmospheric observations. Footprints can be thought of as the sensitivity that an observation had to any upwind emissions in both space and time. Therefore, a single atmospheric observation (y) can be represented by the following relation:

$$y = hx + \epsilon_o + \epsilon_m + \epsilon_b \quad (S1)$$

Where $h \in R^{1\times m}$ is a STILT footprint, $\mathbf{x} \in R^{m\times 1}$ is the true gridded emission vector, ϵ_o is instrument error and ϵ_m is model transport error, and ϵ_b is error in determining the background. Since TROPOMI XCH4 represents a column averaged concentration, we must generate STILT footprints at many altitudes, then take their pressure-weighted average, and finally smooth using the TROPOMI averaging kernel, which is near uniform in the troposphere [3]. Here, we simulate STILT footprints at 50-m, 500-m, and 1000-m above surface, and assume that sensitivity to surface emissions is negligible above these heights.

We collect all TROPOMI XCH4 over our observing domain and remove the background to estimate XCH4 enhancements. For each XCH4 observation, we estimate the background as the 5th percentile of all TROPOMI XCH4 within a 100 km radius of that observation. We simulate STILT footprints for each TROPOMI XCH4 enhancement ($y \in R^{n\times 1}$**)** such that we can expand Equation S1:

$$y = Hx + \epsilon_o + \epsilon_m + \epsilon_b \quad (S2)$$

Where $H \in R^{n\times m}$ is the collection of STILT footprints, also called the Jacobian matrix. Each row of **H** represents a unique STILT pressure-weighted column footprint.

Since we do not know the true emissions x, we employ an atmospheric inversion to estimate these values. Often inverse problems for CH4 have used a Bayesian framework [4], where prior emissions are used to constrain the optimal solution. However, the most recent gridded prior for each basin that includes all sectors dates back to 2012 [5], which could mischaracterize the magnitude and spatial distribution of emissions given rapid changes in many basins since 2012 (e.g., Permian). We apply an alternative approach, called regularized regression that does not rely on a prior [6]. This approach, sometimes called Tikhonov regularization, uses a regularization term (e.g., a flat prior) to stabilize the solution. Here we seek a solution that balances model-data mismatch with the stability of the solution:

$$\hat{x} = \left\{ \|R^{-1/2}(y - Hx)\|_2^2 + \lambda^2 \|x\|_2^2 \right\} \quad (S3)$$

Where **R** is the observational error covariance matrix, and the $\| \bullet \|_2$ term represents the L-2 norm. We find the solution by implementing coordinate-gradient descent [6]. The parameter λ is the regularization term, which can be estimated by analyzing an L-curve [7]. In this process, many

potential solutions are solved using a large array of fixed λ values. The solutions are then visualized on a 2-D plot, where the y-axis represents the first term of the right hand side of Equation S3 (model-data mismatch) and the x-axis represents the second term (L-2 norm of emission vector). The solution that occupies the lowermost left part of the plot (i.e., the "elbow") is considered the optimal solution $\hat{x}$. Figure S6 shows an example of an L-curve, where one can select an appropriate λ value. The error covariance matrix **R** accounts for instrument error (σ_o^2), transport model error (σ_m^2), and error in background determination (σ_b^2), which we assume to be diagonal to speed computation, taking the following form:

$$r_{ii} = \sigma_o^2 + \sigma_m^2 + \sigma_b^2 \quad (S4)$$

TROPOMI column precision is reported to be approximately 0.7%, which translates to roughly 11 ppb. Studies have shown that STILT simulations with high 1 km resolution meteorological data incurs approximately 4 ppb transport error [8]. Given the coarser resolution of HRRR winds, we assume 10 ppb transport error here. We also estimate 17 ppb variability in the background. We populate the entries of **R** using these uncertainty parameters.

We estimate ensemble uncertainty on posterior fluxes by performing inversions following Equation S3 on random samples of **y** for each inversion time period. Reported uncertainties represent the 1σ standard deviation of posterior flux estimates due to random sampling.

Section S2.2: Validation of inversion algorithm

The inversion algorithm described in Section S2.1 can be validated against multiple near-simultaneous fluxes derived from independent observations. These include a tower network in the Uinta Basin [9], a tower network in the Permian (PermianMap.org), and mass-balance flights flown by Scientific Aviation in the Permian (PermianMap.org). For each of these independent flux estimates, we clip our TROPOMI inverse flux grid spatially to match the grid of the independent estimate. We compare our TROPOMI-derived inverse fluxes against these observations in Table S1. Flux estimates from tower networks span time ranges akin to our TROPOMI flux inversions, except for the Uinta, which represents a yearly average. Aircraft mass balance estimates represent a daytime average flux. However, relative differences between flux estimates vary between -36% to 42% across basins and time periods. These relative differences do not exceed the 2σ uncertainties of the TROPOMI flux inversions in any basin.

Table S1 also includes flux estimates for studies carried out asynchronously from our campaigns and where spatial flux domains do not overlap (Marcellus, Denver-Julesburg). These cannot be used for direct validation of our inversion approach, but are still useful for comparison. Relative differences between these campaigns and our flux estimates vary between -18% to 43%, again within 2σ uncertainties of our flux estimates. Finally, Table S2 lists the retrieval parameters and data density of TROPOMI retrievals that were used for each basin inversion.

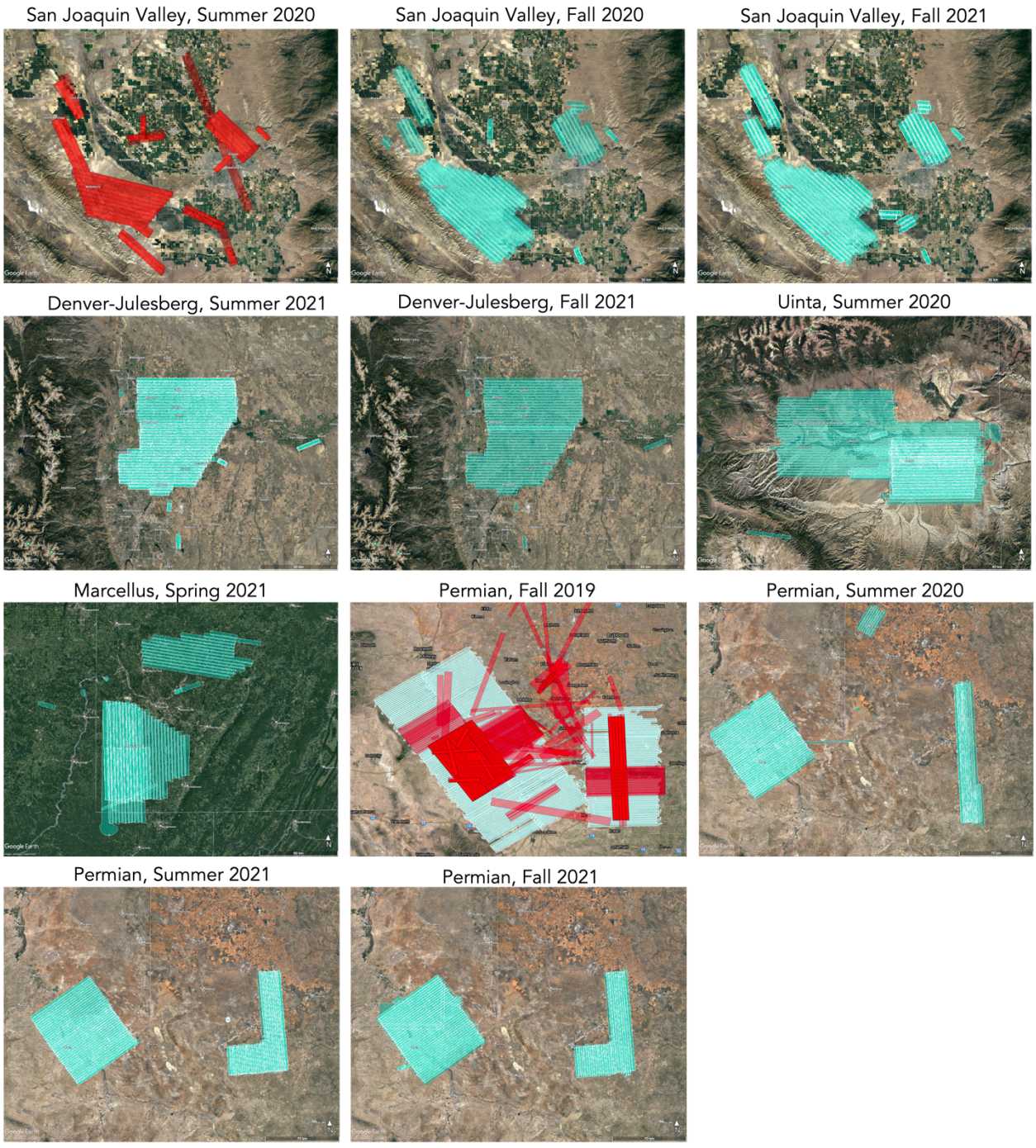

Figure S1. Flight lines overflown for each of the campaigns described in the survey. Red coloring indicates lines that were flown with AVIRIS-NG. Teal coloring indicates lines that were flown with GAO.

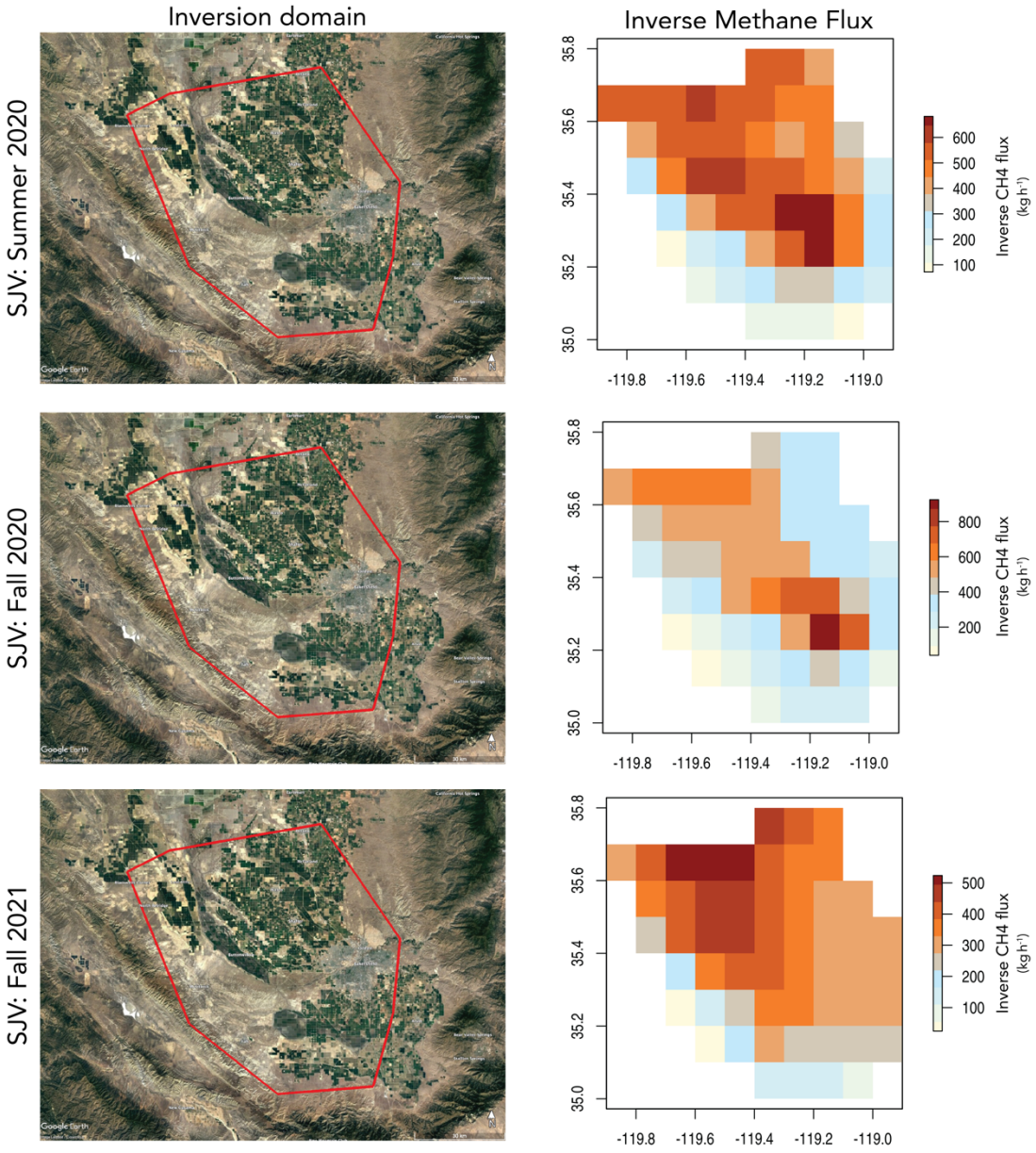

Figure S2. Regional TROPOMI-based flux inversions for the indicated basins and time periods. Note that the colorbars are not consistent.

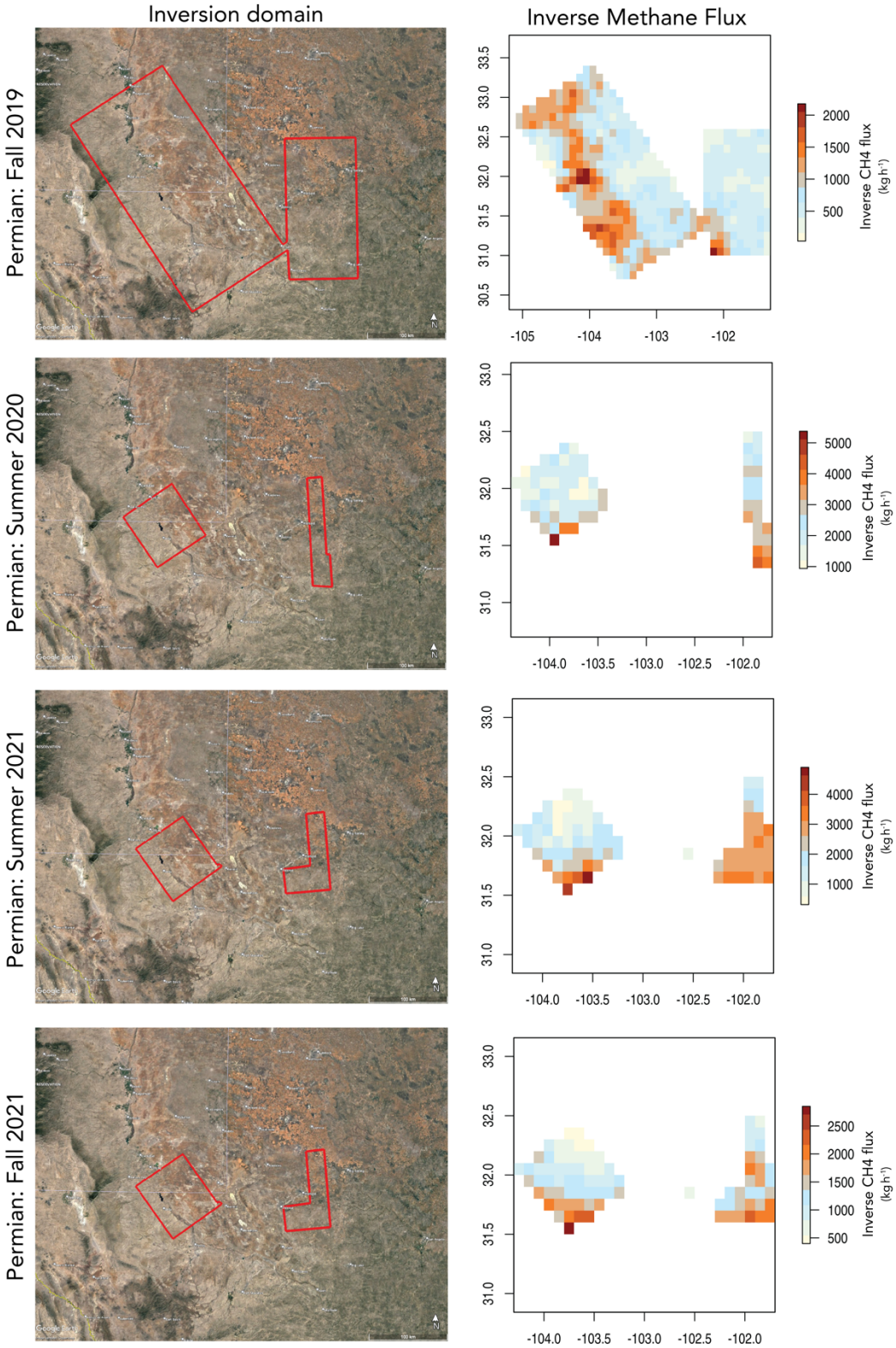

Figure S3. Regional TROPOMI-based flux inversions for the indicated basins and time periods. Note that the colorbars are not consistent.

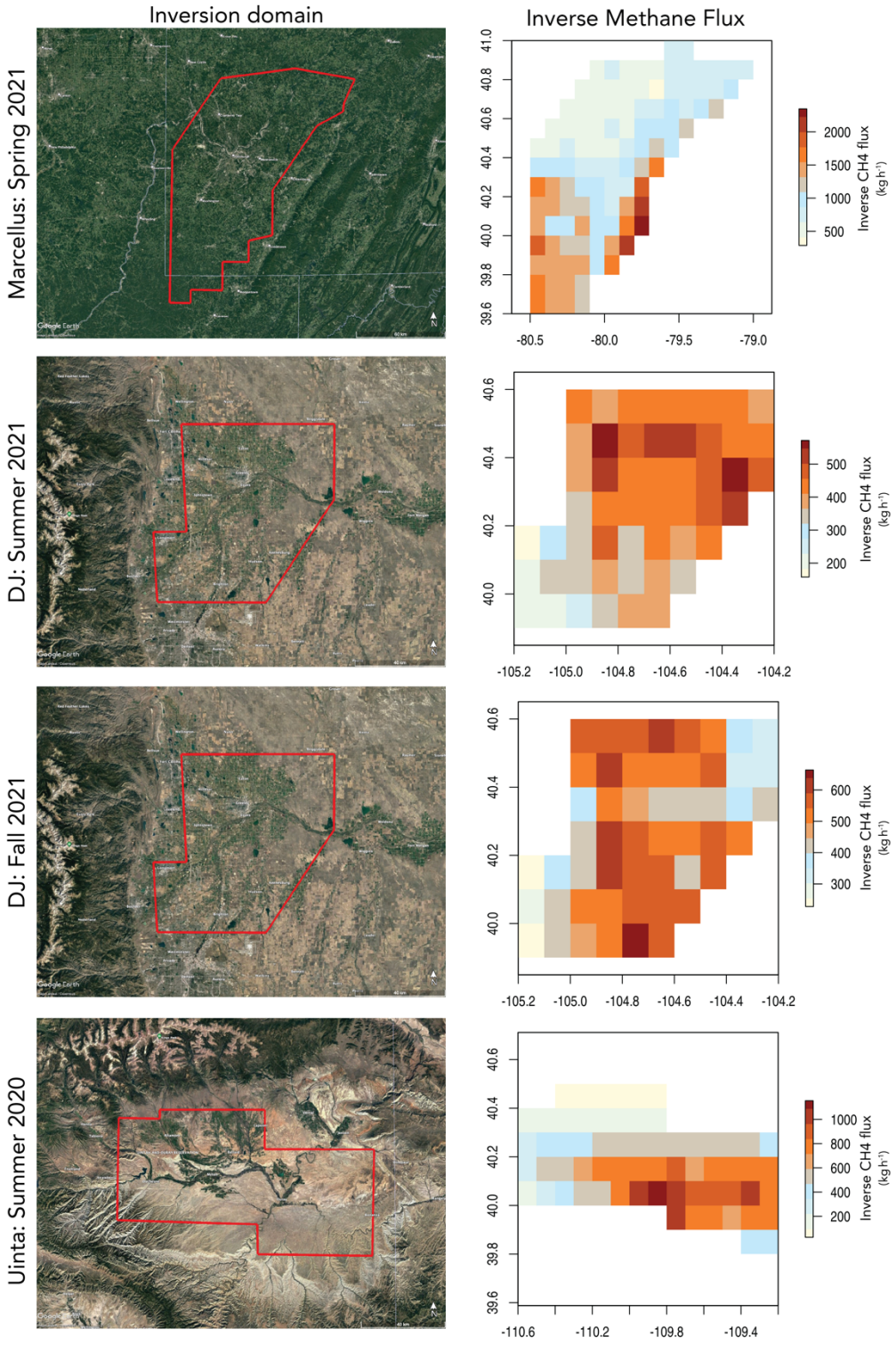

Figure S4. Regional TROPOMI-based flux inversions for the indicated basins and time periods. Note that the colorbars are not consistent.

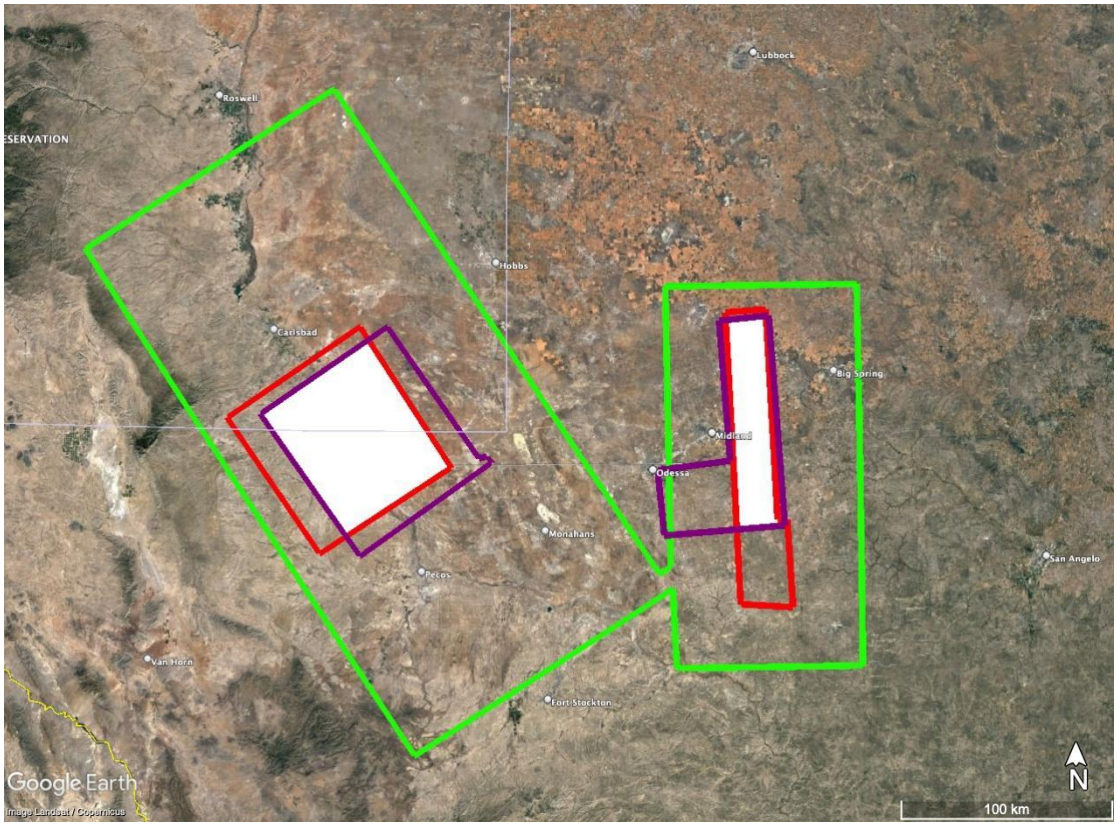

Figure S5. Domains for the Permian that correspond to the convex hull of airborne overflights (Figure S1, S3). The inner white boxes represent the region of overlap across campaigns that were used to assess trends in aggregated point source budgets.

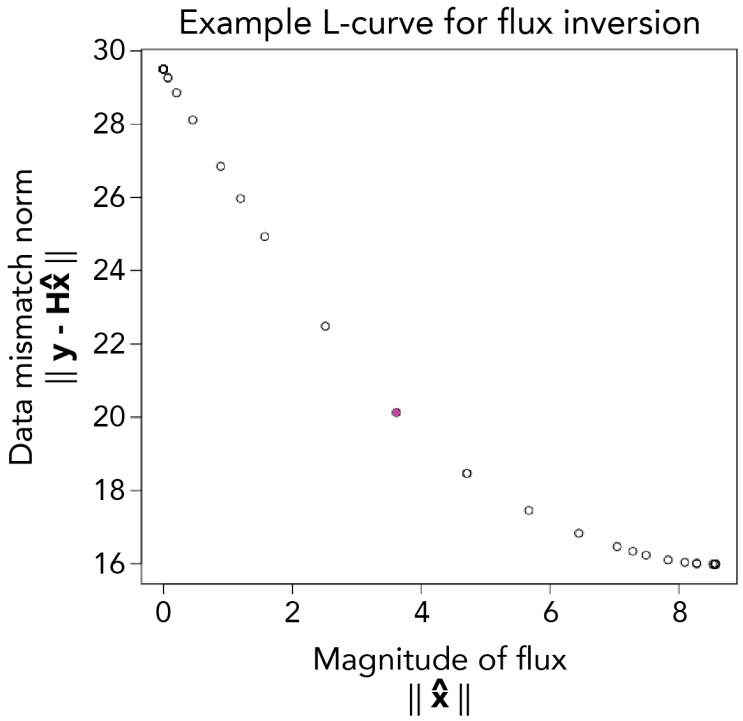

Figure S6. Example L-curve described in Section S2.1 that is used to identify an optimal regularization parameter (purple dot) for L-2 regularized regression.

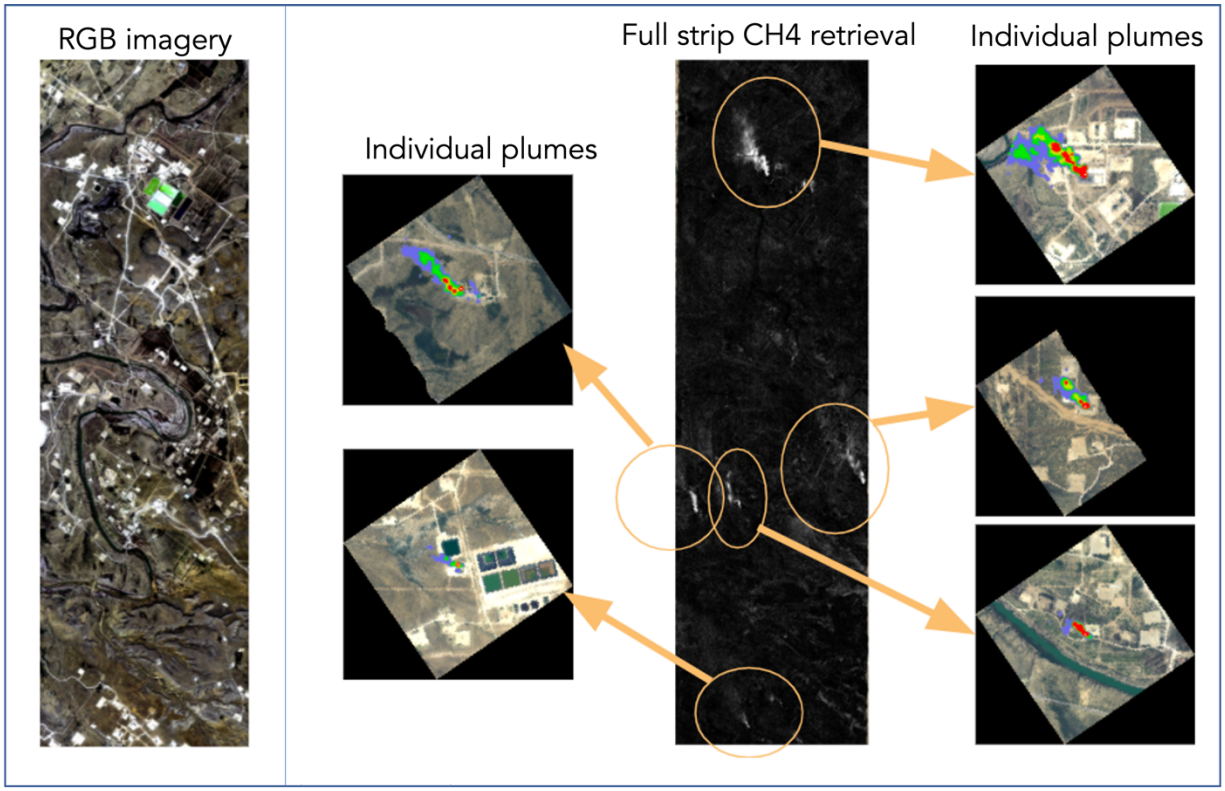

Figure S7. Example of full scene collect from AVIRIS-NG. The left panel shows RGB imagery from AVIRIS-NG. The right panel shows the full strip CH4 retrieval (black and white) that is used to identify plume geolocations, which are then used to generate unique plume imagery and quantify emissions.

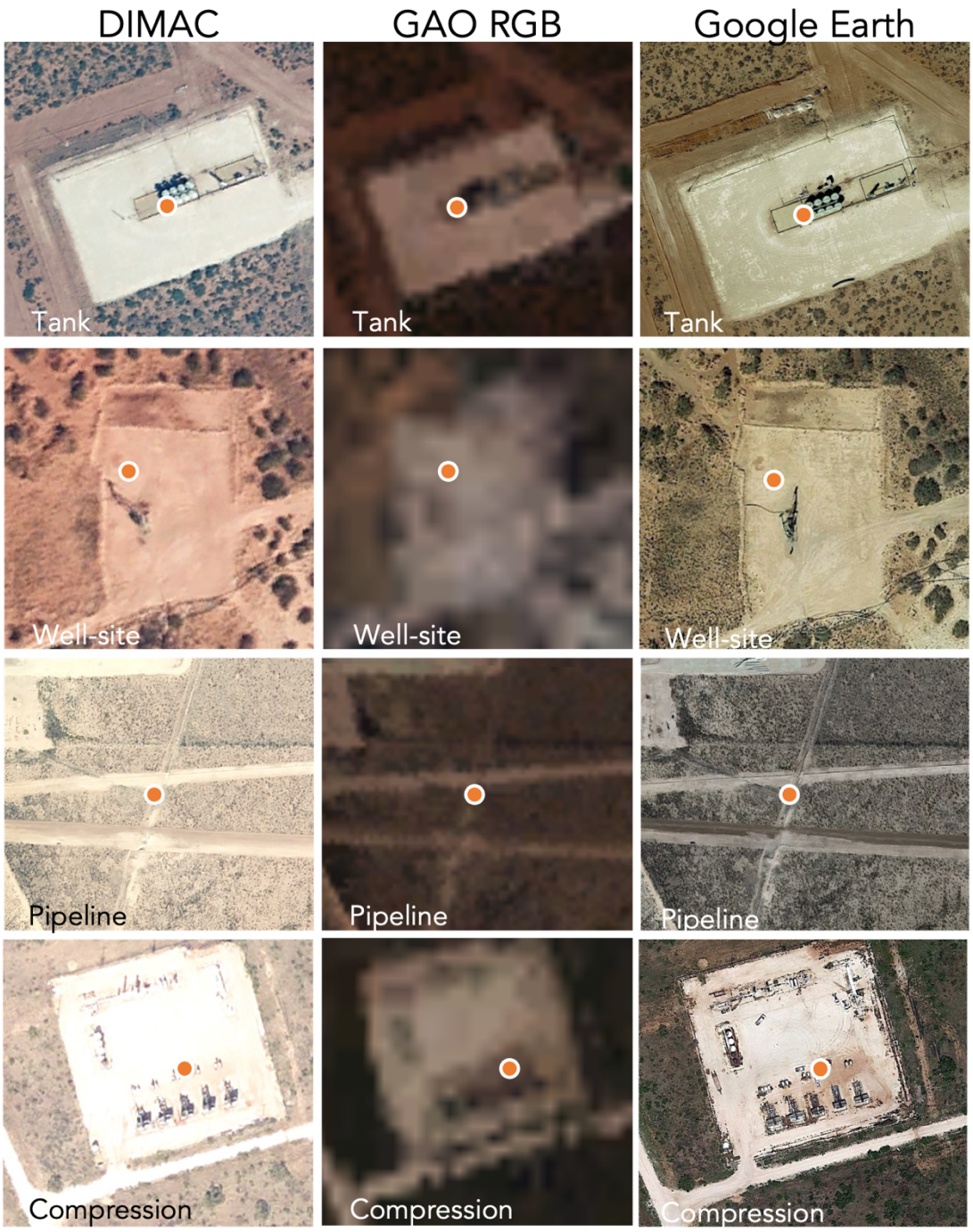

Figure S8. Examples of source attributions that were performed using GAO RGB, DIMAC, and Google Earth.

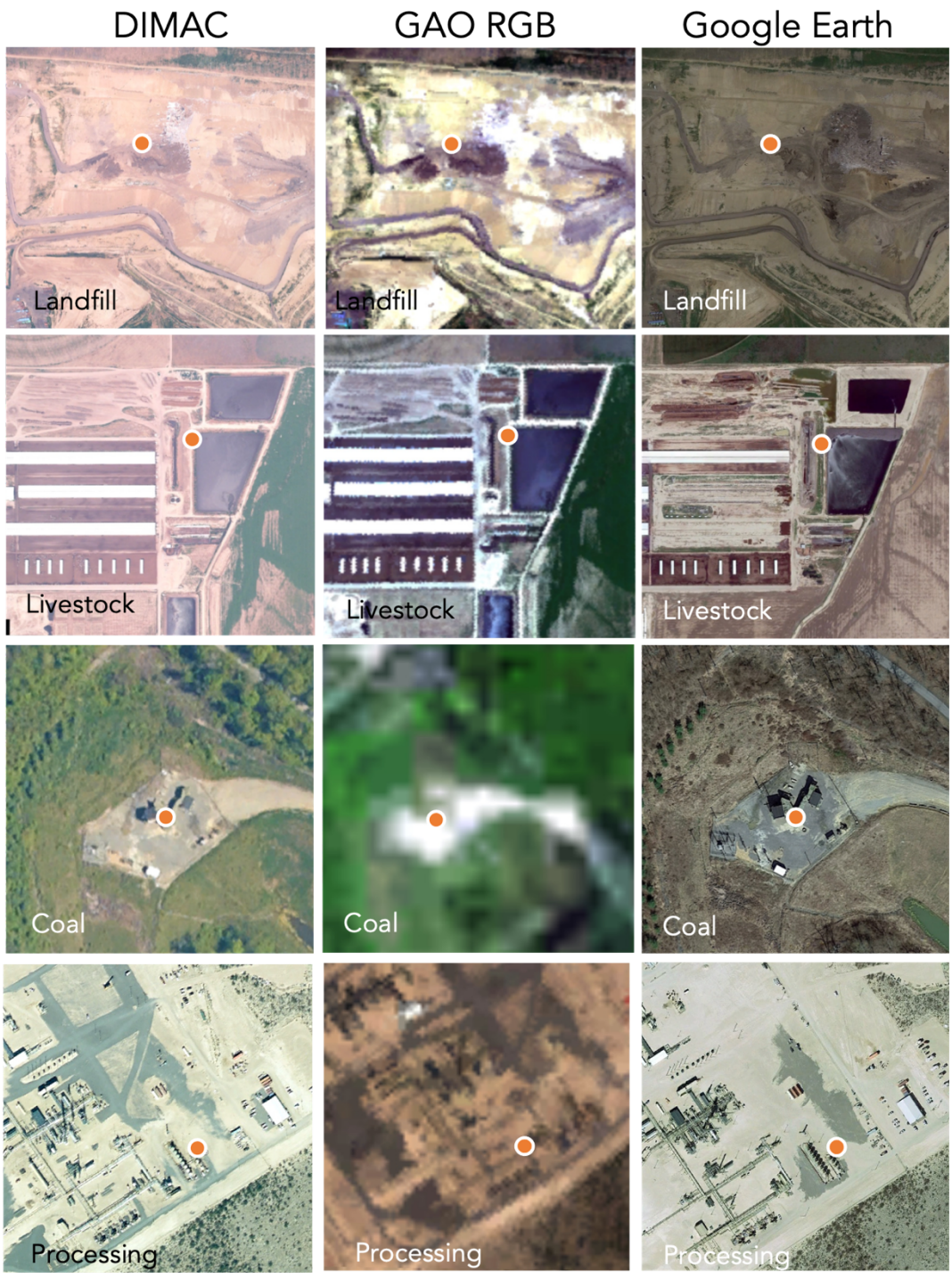

Figure S9. Examples of source attributions that were performed using GAO RGB, DIMAC, and Google Earth.

Table S1: Validation of TROPOMI XCH4 flux inversion

Basin	TROPOMI inversion time period	TROPOMI derived CH4 fluxes (t CH4 h^{-1})	Independent measurement system[a]	Independent measurement system time period	Independent flux rate (t CH4 h^{-1})	Difference relative to independent flux estimate
Spatial / Temporal Overlapping studies						
Permian	Sep-Nov 2019	107 ± 43	Aircraft mass-balance	Oct 17, 2019	167 ± 31	-36%
Permian	July-Aug 2020	118 ± 25	Tower network	July-Aug 2020	142	-17%
Permian	July-Aug 2020	118 ± 25	Aircraft mass-balance	Jul 13, 2020	123	-4%
Permian	July-Aug 2021	112 ± 27	Tower network	July-Aug 2021	134	-16%
Uinta	July-Aug 2020	33.9 ± 5.5	Tower network	2020	24	42%
Non-Spatial / Temporal Overlapping studies						
Denver-Julesburg	June-July 2021	21.1 ± 4.1	Aircraft mass-balance[b]	2 flights: May 2012	26.0 ± 7.4	-18%
Denver-Julesburg	Sep-Oct 2021	25.2 ± 6.8	Aircraft mass-balance	2 flights: May 2012	26.0 ± 7.4	-3.1%
Marcellus	May-Jun 2021	109 ± 39	Aircraft mass-balance[c]	3 flights; Aug-Sep 2015	76.3 ± 7.2	43%

[a]Independent flux estimates from the Permian were retrieved from the Environmental Defense Fund's PermianMAP (PermianMap.org). Flux estimates from the Uinta Basin can be found in Lin et al. [9], https://doi.org/10.1038/s41598-021-01721-5
[b]Petron et al., [10], https://doi.org/10.1002/2013JD021272
[c]Ren et al., [11], https://doi.org/10.1029/2018JD029690

Table S2: TROPOMI data density and retrieval parameters/observing conditions for each inversion

Basin	Inversion time period	Area of inversion domain (km^2)	Number of observations	Average Shortwave Infrared Albedo	Average Aerosol Optical Thickness	Average Surface Altitude (m)
San Joaquin Valley	July-Sep 2020	5.60E+03	7.59E+03	1.98E-01	2.04E-02	1.95E+02
San Joaquin Valley	Oct-Nov 2020	5.60E+03	5.83E+03	1.98E-01	1.78E-02	1.83E+02
San Joaquin Valley	Oct-Nov 2021	5.60E+03	5.21E+03	2.10E-01	2.89E-02	1.83E+02
Permian	Sep-Nov 2019	5.40E+04	2.99E+04	2.35E-01	4.39E-02	1.01E+03
Permian	July-Aug 2020	8.40E+03	9.20E+03	2.70E-01	6.82E-02	9.24E+02
Permian	July-Aug 2021	8.90E+03	6.79E+03	2.36E-01	5.65E-02	9.08E+02
Permian	Sep-Oct 2021	8.90E+03	1.14E+04	2.46E-01	2.77E-02	9.10E+02
Uinta	July-Aug 2020	6.20E+03	3.99E+03	2.58E-01	1.73E-01	1.67E+03
Denver-Julesburg	June-July 2021	4.80E+03	5.85E+03	1.80E-01	4.88E-02	1.52E+03
Denver-Julesburg	Sep-Oct 2021	4.80E+03	4.44E+03	1.88E-01	4.97E-02	1.53E+03
Southwest Pennsylvania	May-Jun 2021	1.03E+04	2.84E+03	8.12E-02	5.64E-02	3.70E+02

SI References

Sample References:

1. Cusworth, D.H., Duren, R.M., Thorpe, A.K., Olson-Duvall, W., Heckler, J., Chapman, J.W., Eastwood, M.L., Helmlinger, M.C., Green, R.O., Asner, G.P. and Dennison, P.E., 2021. Intermittency of large methane emitters in the Permian Basin. *Environmental Science & Technology Letters*, *8*(7), pp.567-573.
2. Fasoli, B., Lin, J.C., Bowling, D.R., Mitchell, L. and Mendoza, D., 2018. Simulating atmospheric tracer concentrations for spatially distributed receptors: updates to the Stochastic Time-Inverted Lagrangian Transport model's R interface (STILT-R version 2). *Geoscientific Model Development*, *11*(7), pp.2813-2824.
3. Veefkind, J.P. *et al*. TROPOMI on the ESA Sentinel-5 Precursor: A GMES mission for global observations of the atmospheric composition for climate, air quality and ozone layer applications. *Remote sensing of environment*, *120*, 70-83. (2012)
4. Rodgers, C.D., 2000. *Inverse methods for atmospheric sounding: theory and practice* (Vol. 2). World scientific.
5. Maasakkers, J.D. *et al*. Gridded national inventory of US methane emissions. *Environmental science & technology*, *50*(23), pp.13123-13133. (2016)
6. Friedman, J., Hastie, T. and Tibshirani, R., 2010. Regularization paths for generalized linear models via coordinate descent. *Journal of statistical software*, *33*(1), p.1.
7. Hansen, P.C. and O'Leary, D.P., 1993. The use of the L-curve in the regularization of discrete ill-posed problems. *SIAM journal on scientific computing*, *14*(6), pp.1487-1503.
8. Cusworth, D.H., Jacob, D.J., Sheng, J.X., Benmergui, J., Turner, A.J., Brandman, J., White, L. and Randles, C.A., 2018. Detecting high-emitting methane sources in oil/gas fields using satellite observations. *Atmospheric Chemistry and Physics*, *18*(23), pp.16885-16896.
9. Lin, J.C., Bares, R., Fasoli, B., Garcia, M., Crosman, E. and Lyman, S., 2021. Declining methane emissions and steady, high leakage rates observed over multiple years in a western US oil/gas production basin. *Scientific reports*, *11*(1), pp.1-12.
10. Pétron, G., Karion, A., Sweeney, C., Miller, B.R., Montzka, S.A., Frost, G.J., Trainer, M., Tans, P., Andrews, A., Kofler, J. and Helmig, D., 2014. A new look at methane and nonmethane hydrocarbon emissions from oil and natural gas operations in the Colorado Denver-Julesburg Basin. *Journal of Geophysical Research: Atmospheres*, *119*(11), pp.6836-6852.
11. Ren, X., Hall, D.L., Vinciguerra, T., Benish, S.E., Stratton, P.R., Ahn, D., Hansford, J.R., Cohen, M.D., Sahu, S., He, H. and Grimes, C., 2019. Methane emissions from the Marcellus Shale in Southwestern Pennsylvania and Northern West Virginia based on airborne measurements. *Journal of Geophysical Research: Atmospheres*, *124*(3), pp.1862-1878.